DNS and modeling of the turbulent boundary layer over an evaporating liquid film

Gaëtan Desoutter [a],[1], Chawki Habchi [a],[*], Bénédicte Cuenot [b], Thierry Poinsot [c]

[a] *IFP, 1 & 4 Avenue Bois-préau, 92852 Rueil-Malmaison cedex, France*
[b] *CERFACS, 42 Avenue Gaspard Coriolis, 31057 Toulouse Cedex 01, France*
[c] *IMFT (UMR CNRS-INPT-UPS 5502), Toulouse, France*

ABSTRACT

Contrary to the case of flame interaction with a dry wall, little is known today about liquid film evaporation effects on the physics and structure of the boundary layer and on the flame evolution when approaching a liquid film. In this paper, Direct Numerical Simulation (DNS) is used to study the boundary layer above a liquid evaporating film in the fully developed turbulent channel flow configuration where only the liquid film surface is viewed by the simulation through a boundary condition. First, the classical minimal isothermal channel of Kim et al. [J. Kim, P. Moin, R. Moser, Turbulence statistics in fully developed channel flow at low Reynolds number, J. Fluid Mech. 177 (1987) 133–166] is computed to check the accuracy of the DNS solver. Next, the calculations are repeated for an anisothermal case where hot gas is flowing between cold walls. The numerical results corroborate those of Nicoud [F. Nicoud, G. Winckelmans, D. Carati, J. Baggett, W. Cabot, Boundary conditions for LES away from the wall, in: Summer Program, Center for Turbulence Research, 1998, pp. 413–422] and Huang & Coleman [P. Huang, G. Coleman, Van driest transformation and compressible wall-bounded flows, AIAA J. 32 (10) (1994) 2110–2113], introducing modified dimensionless variables. Finally, an evaporating liquid film is added at the walls. The complexity of the interaction between the evaporation process and the boundary layer structure, as well as its strong dependence on the thermophysical properties (that change with the mixture composition) are highlighted. As in the anisothermal case, the classical wall units are no longer adapted to build wall functions and new dimensionless variables are proposed. In addition a wall function must be developed for the evaporating species mass fraction, using a new dimensionless wall variable. It is shown that using these new variables allows to derive new wall functions for momentum, temperature and mass that lead to a correct description of the boundary layer when compared to DNS. These new wall functions may be directly implemented in CFD codes to take into account the impact of an evaporating liquid film.

1. Introduction

The formation of liquid films on walls is encountered in many engineering applications, such as air coolers, cooling towers, drying processes or Gasoline Direct Injection (GDI) engines. GDI technology is developed today as an alternative technology to lower the fuel consumption together with pollutant emissions, which are both crucial topics for the future. In these engines the fuel spray may impinge on the piston and form a liquid fuel film on its surface (Fig. 1). The evaporation of this liquid film and its interaction with the flame that may lead to flame quenching and production of unburnt hydrocarbons (HC) then alter the engine operation and performance. In spite of their widespread applications, simultaneous

heat and mass transfer between a liquid film and a turbulent air stream have not been much investigated. In the case of GDI engines the generic configuration is actually very complex as it involves a flame that may approach the liquid film and interact with it. Being able to model this interaction is therefore a key issue in CFD codes.

Most approaches for wall-bounded flows are based on wall functions [5], originally developed for simple homogeneous gaseous flows and describing both the dynamic and the thermal fluxes. This approach was later extended to complex configurations such as transpiration through walls [6,7]. More recently, the turbulent flow around a cooling multiperforated plate was studied to derive a wall function able to reproduce the main characteristics of such a complex flow [7]. Intially developed for small temperature differences between the flow and the wall (to keep small density and viscosity variations) [8], the thermal wall function was later extended to strongly anisothermal situations [6]. Another usual assumption is that the flow composition in the channel is frozen and may be described with one single species. This is however

* Corresponding author. Tel.: +33 1 47526151; fax: +33 1 47527068.
  E-mail address: Chawki.HABCHI@ifp.fr (C. Habchi).
[1] Present address: CD-adapco, Paris office, 31 rue Delizy, 93698 Pantin Cedex, France.

Nomenclature

C, K	constants
D	diffusion coefficient
h	channel half-width
L	length
$\dot{M}$	mass flow rate
P	pressure
Pr	Prandtl number
Re	Reynolds number
S	source term
Sc	Schmidt number
T	temperature
U	streamwise velocity
W	molecular weight
x	mol fraction
Y	mass fraction
(u, v, w)	velocity components
(x, y, z)	position components

Superscripts

s	wall or liquid film surface
$+$	non-dimensional
sat	saturation conditions

Abbreviations

AVBP	LES and DNS code developed by CERFACS and IFP
DNS	Direct Numerical Simulation
KMM	paper of Kim J., Moin P. and Moser R.
TTGC	third-order in time and space numerical scheme in AVBP

Greek symbols

$\alpha = v/Pr$	thermal diffusivity
φ	heat flux
(η, ϕ, θ)	LnKC variables
λ	heat conductivity coefficient
v	kinematic viscosity
ρ	density
τ	shear stress

Subscripts

c	center of the channel
eff	effective value
E	energy
F	fuel
k	fuel or air species
kin	kinetic
int	internal
lam	laminar
lt	laminar-turbulent
M	mass
max	maximum value
rms	root-mean-square value
S	Stephan speed
$t, turb$	turbulent
$target$	target value
w	wall

not true in combustion applications where chemical reactions modify the mixture composition up to the wall, and wall functions were again extended in this context to account for mass fraction variations [9]. Moreover the extension to reacting flows requires the modelling of the flame behaviour when approaching the wall and its impact on the wall fluxes. This was done by several authors [10,11], who identified the flame quenching distance and calculated the resulting wall fluxes. The case of chemically reacting walls (leading to ablation for example) was also studied by Artal et al. [12]. All these studies assume a purely gaseous flow and a

Fig. 1. Fuel injection and liquid film formation on the surface of the piston of Gasoline Direct Injection (GDI) engines.

dry wall. The description of a liquid film in such models remains today a challenge.

A powerful method to study, design and validate wall functions is Direct Numerical Simulation (DNS) that has been often used in the last twenty years and in most of the works cited above. The methodology uses theoretical arguments to build generic formulas for mean and fluctuating velocity profiles near the wall [13] and DNS is used to verify the validity of the underlying assumptions. In a second step the developed wall laws are confronted to DNS results on representative flows for validation and fitting the constant parameters involved in the formulas.

In this paper, the above methodology (DNS combined with theory) is used to study the interaction between an evaporating liquid film and the turbulent boundary layer created in the vicinity of a wall in the generic configuration of the periodic turbulent channel flow. The liquid film flow is not solved but only its impact on the gaseous boundary layer is studied, through the boundary condition that reflects the film surface properties. The objective is to give a detailed understanding and build a model of the boundary layer structure above the film surface. In this two-way interaction, the liquid film evaporation is influenced by the near-wall gradients of species and the wall temperature, while the mass flux due to evaporation blows the boundary layer away from the wall, thereby changing the flow profiles and deviating significantly from the classical wall functions. It has been shown in previous studies that the boundary layer structure and more specifically the distance between the wall and the laminar-turbulent transition depend on the velocity of wall injection [6,14,15]. In this work, a broad range of Stephan velocity is considered to establish the physics of the coupling between the turbulent flow and the evaporating film. New wall functions are then designed, to take into account both anisothermicity and film evaporation effects.

The paper is organized as follows: Section 2 presents the characteristics of the turbulent channel flow with and without evap-
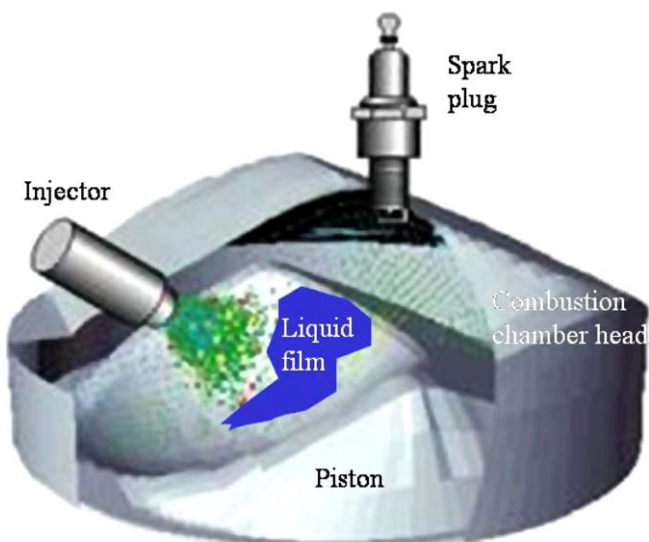
orating liquid films on walls. Next, the numerical approach is detailed in Section 3, describing in particular the source terms methodology to handle the periodic channel imposing zero net mass, momentum and energy total balances. The classical isothermal flow case is presented in Section 4, followed by the anisothermal flow case discussed In Section 5. Then, Section 6 presents and analyses the DNS results obtained for the channel flow with evaporating liquid films, and the new wall functions for fuel vapor mass fraction, gas velocity and temperature are derived and compared to DNS.

2. Configuration

Jimenez and Moin [16] proved that the low-order turbulence statistics obtained by simulating the flow in a minimum plane channel are in good agreement with experiments in the near-wall region for boxes wider (respectively longer) than approximately 100 (respectively 350) wall units in the spanwise (respectively streamwise) direction. This important result allows to limit the domain size and therefore the computing time, and the so-called "minimal channel" configuration was often chosen in previous works. The same configuration is used here, as illustrated on Fig. 2. The top and bottom boundaries of the computational box are either isothermal no-slip walls or liquid films, while the boundaries in both the streamwise and the spanwise directions are periodic. The gas flow consists of an inhomogenous mixture of air and heptane with an average pressure of one bar whereas the liquid phase is pure heptane.

Note that in the following and throughout the paper, all quantities with a ($^+$) superscript, a (^{s}) superscript, or an overbar correspond respectively to wall units, wall or film surface values, or represent (x,z)-plane and time averages. In all computations, the mean centerline velocity $\overline{U_c} \approx 50$ m s^{-1}, and the Reynolds number Re – based on $\overline{U_c}$, the centerline kinematic viscosity ν_c and the channel half-width h – lies between 2700 and 3300. The Reynolds number Re_τ based on h, the shear velocity $u_\tau = \sqrt{\tau^s/\rho^s}$, with τ^s and ρ^s being the mean shear stress and the density, and the kinematic viscosity ν^s, all taken at the wall or the liquid film surface, is typically above 180. The dimensions of the domain are $L_x = \pi h$, $L_y = 2h$ and $L_z = 0.3\pi h$ in the streamwise, normal and spanwise directions respectively, i.e. $L_x^+ \geqslant 565$, $L_y^+ \geqslant 360$ and $L_z^+ \geqslant 169$ in wall units, i.e. $L_i^+ = L_i u_\tau/\nu^s$. As shown by Jimenez and Moin [16] for isothermal flows, these box dimensions are sufficiently large to ensure the development of enough turbulent structures to obtain low order statistics in good agreement with experiments. This assumption will be verified a posteriori in the case of evaporating liquid films. The computational grid is regular in (x,z) directions and the grid spacing $\Delta x^+ \approx 35$ and $\Delta z^+ \approx 5$ is sufficient to resolve the expected elongated structures of turbulence. A grid stretching is used in the normal direction to allow a good

resolution of the near wall viscous sublayer. The grid step verifies $1 \geqslant \Delta y_w^+ \geqslant 0.5$ at the wall or liquid film surface and $\Delta y_c^+ \approx 5$ near the centerline.

3. Numerical method

All the simulations of the present study were carried out with the AVBP code [1] which uses a cell-vertex finite-volume method and solves the compressible conservation equations on arbitrary unstructured grids for the conservatives variables (mass density, momentum, total energy and mass species). It is fully parallel, dedicated to Large-Eddy Simulations (LES) and Direct Numerical Simulations (DNS), and has been widely used and validated in many different configurations over the past years [17–20]. The numerical scheme is a Taylor–Galerkin scheme (TTGC) [21] that is third-order in time and space.

To compute a statistically steady configuration in a periodic channel, source terms must be added to the momentum, total energy and heptane mass fraction equation. These source terms are designed to compensate for the effects of the wall or liquid film shear stress, heat flux and mass evaporation. The constant force S added to the streamwise momentum equation is:

$$S = K_S \frac{\rho^s U_{max}^2}{h} \tag{1}$$

where $U_{max} = \overline{U_c} = 50$ m s^{-1} and K_S is a constant adjusted to reach $\overline{U_c} \approx U_{max}$. Consistently, a source term $S.u$ is added to the total energy equation, where u is the streamwise velocity component.

The constant heat source S_E added to the total energy equation is:

$$S_E = \langle \rho C_\nu \rangle \frac{(T_{target} - \langle T \rangle)}{\tau_t} \tag{2}$$

where C_ν is the mass specific heat capacity at constant volume, T_{target} is a target temperature and $\langle \rangle$ denotes the volumic average operator over the whole domain. $\tau_t \approx h/2u_\tau$ is a characteristic time of turbulent diffusion.

The constant mass source S_M added to the heptane mass fraction equation is:

$$S_M = \langle \rho \rangle \frac{\left(Y_{F\,target} - \frac{\langle \rho Y_F \rangle}{\langle \rho \rangle} \right)}{\tau_t} \tag{3}$$

where $Y_{F\,target}$ denotes a target heptane mass fraction. Consistently, the momentum source terms $S_M.u_i$ and the energy source term $S_M \cdot [E_{int} + E_c]$ are respectively added to the momentum equations and the total energy equation. E_{int} and E_c are respectively the internal energy of heptane and the kinetic energy. Note that S_M is always a negative term because it compensates for the mass introduced in the computational domain through evaporation. The different source terms are summarized in Table 1.

For the purpose of the present study, there is no need to explicitely introduce a liquid film in the calculation. Indeed the interaction of the liquid film with the flow is essentially located at the film surface, and only the surface properties of the film are needed.
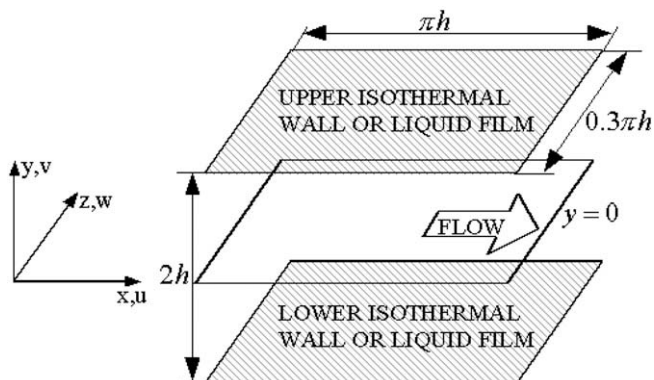

Fig. 2. Computational domain and coordinate system. Note that the simulation is periodic in both x- and z-directions.

Table 1
Source terms added to the conservative equations of the gas.

Source terms			
Equations			
Streamwise momentum	S		$S_M.u$
Normal momentum			$S_M.\nu$
Spanwise momentum			$S_M.w$
Total energy	$S.u$	S_E	$S_M.[E_{int} + E_{kin}]$
Heptane mass density			S_M

Table 2
Liquid film boundary condition.

Temperature	$T^s = Constant$	
Mass fractions	$Y_F^s = P_F W_F / P^s W^s,$	$Y_{air}^s = 1 - Y_F^s$
Velocity	$v^s = \frac{\dot{M}}{\rho^s} = v_S,$	$u^s = w^s = 0$

Table 3
Thermochemical and transport properties of the mixture in non-evaporating cases. Air is considered as a mixture of Oxygen O_2 and Nitrogen N_2.

W	v (300 K)	v (600 K)	Pr	Sc
33.6 g mol^{-1}	1.17 10^{-5} m^2 s^{-1}	1.63 10^{-5} m^2 s^{-1}	0.78	1.65

Therefore the film is simply represented by a boundary condition for the gaseous flow, that imposes the film surface temperature T^s to a constant value, the mass fractions Y_k^s to the saturation values of a mixture of air and heptane at one bar, and the normal velocity to the Stephan velocity v_S (Table 2). The saturated fuel vapor mass fraction Y_F^s is calculated from the Clausius–Clapeyron relation and the Raoult's relation as $Y_F^s = P_F^{sat}(T^s)W_F/P^s W^s$, and the associated air mass fraction is simply $Y_{air}^s = 1 - Y_F^s$. The Stephan velocity is calculated from the evaporated mass flow rate of heptane $\dot{M}$ given by [22]:

$$\dot{M} = \rho^s v_S = \frac{\rho^s v^s}{(1 - Y_F^s)Sc}\left(\frac{\partial Y_F}{\partial y}\right)^s \quad (4)$$

where Sc is a Schmidt number that represents the diffusion velocity of heptane in a heptane–air mixture. It is calculated as:

$$\frac{1}{Sc} = W\left[\frac{1 - Y_F}{W_{air}Sc_F} + \frac{Y_F}{W_F Sc_{air}}\right] \quad (5)$$

where W is the mean molecular weight, W_k is the molecular weight of species k and Sc_k is the Schmidt number of species k. In Eq. (4) the fuel vapor gradient at the film surface is unknown a priori and is evaluated from the simulation.

4. Isothermal flow

The results obtained for the classical 'minimum channel' configuration are presented and compared to the results of Kim et al. [2] (below referred to as 'KMM') considered as a reference. In the present case the top and bottom boundaries of the computational box are isothermal no-slip walls at temperature $T^s = 300$ K (Fig. 2). The gas is a mixture of heptane and air also at $\overline{T} = 300$ K and one bar, with a uniform fuel mass fraction of $\overline{Y}_F = 0.2$. The corresponding thermochemical and transport properties are given in Table 3 where P_r denotes the Prandlt number. The channel half-width is $h = 0.77031 \times 10^{-3}$ m, leading to the Reynolds numbers $Re \approx 3300$ and $Re_\tau \approx 180$ as in the DNS of KMM [2]. The computational grid is $18 \times 120 \times 36$ with a stretching in the direction normal to the walls, corresponding to a grid spacing of $\Delta x^+ \approx 33.4, \Delta y_w^+ \approx 1.0, \Delta y_c^+ \approx 4.9$ and $\Delta z^+ \approx 4.9$. All statistics are calculated from (x, z)-plane and time averages, over a time corresponding to $790h/\overline{U}_c$.

The mean velocity profile $\overline{u}^+ - u^s = \overline{u}/u_\tau$ is shown in Fig. 3a. It is in very good agreement with the result of KMM [2] and is correctly modelled by a linear law ($\overline{u}^+ = y^+$) in the viscous laminar sublayer and by a standard logarithmic law ($\overline{u}^+ = 2.5ln(y^+) + 5.5$) in the above inertial zone of the boundary layer. In the fully developed
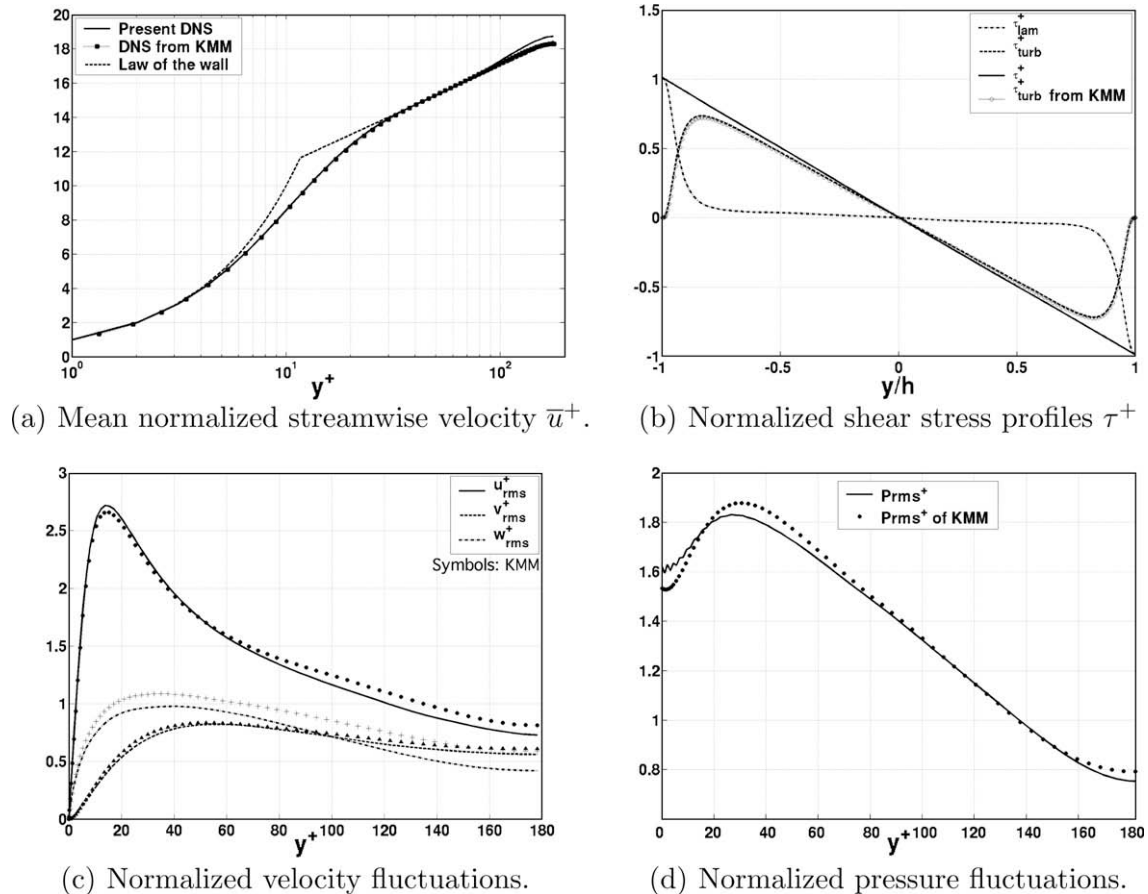

(a) Mean normalized streamwise velocity $\overline{u}^+$.

(b) Normalized shear stress profiles τ^+

(c) Normalized velocity fluctuations.

(d) Normalized pressure fluctuations.

Fig. 3. Isothermal flow results. Comparison with results of [2] (KMM).

turbulence channel flow considered here, the total shear stress τ^+ should be a linear function of the normal coordinate y^+:

$$\tau^+ = \tau^+_{turb} + \tau^+_{lam} = -\overline{u'v'}^+ + \frac{\partial \bar{u}^+}{\partial y^+} \approx -\frac{y^+}{h^+} \qquad (6)$$

where it is assumed that τ^+_{lam} has a negligible contribution. Fig. 3b shows that the above relation is well satisfied, indicating that the flow has reached a statistically steady state. Moreover, the Reynolds shear stress τ^+_{turb} is also in excellent agreement with the result of KMM [2]. Turbulent intensities $u^+_{rms} = \sqrt{\overline{u'^2}}/u_\tau$, $v^+_{rms} = \sqrt{\overline{v'^2}}/u_\tau$ and $w^+_{rms} = \sqrt{\overline{w'^2}}/u_\tau$ are shown in Fig. 3c. The agreement with the DNS of KMM is quantitatively good for the streamwise and normal velocity fluctuations, especially near the wall, but only qualitatively correct for the spanwise velocity fluctuation. The differences are mainly due to the small width of the computational box and the weak resolution around the channel centerline, together with the dissipation of the numerical scheme. Fig. 3d shows the profile of pressure fluctuations normalized by the wall shear velocity, $P^+_{rms} = P_{rms}/\rho u^2_\tau$. A maximum deviation from the result of KMM of about 7 % is obtained (see Fig. 3).

This set of results validates the numerical approach and allows to consider the anisothermal flow, presented in the next section.

5. Anisothermal flow

In this section the DNS of a heated gas flowing between two cold walls is performed in order to observe the behavior of the laws of the wall in the presence of a temperature gradient. In the pres-

ent case, the gas is heated to $\overline{T}_c = 600$ K (where $\overline{T}_c$ denotes the mean centerline temperature) while the top and bottom boundaries are isothermal no-slip walls at temperature $T^s = 360$ K. The gas composition is as in the isothermal case, with the same thermochemical and transport properties (Table 3) except for the viscosity v that increases with the temperature. The channel half-width is $h = 2.3731 \times 10^{-3}$ m, leading to the Reynolds numbers $Re \approx 3000$ and $Re_\tau \approx 300$. The computational grid is $19 \times 150 \times 38$, stretched in the normal direction so that $\Delta x^+ \approx 52.6$, $\Delta y^+_w \approx 0.8$, $\Delta y^+_c \approx 7.7$ and $\Delta z^+ \approx 7.7$. Statistics were collected over a time sample of roughly $560h/\overline{U}_c$. The quality of the simulation is first checked with sample streamwise and spanwise velocity power spectra shown in Fig. 4a and b. The drop-offs at high frequencies guarantee that the small scales are adequately represented. Fig. 4c and d show the two-point spatial autocorrelation functions for the velocity field in the near-wall region ($y^+ = 5.5$). These autocorrelation functions do not exactly reach zero at the largest separation distances, but the levels are reasonable. In addition, these function levels are close to the isothermal case of previous studies [16], showing sufficient domain size and grid resolution for near-wall turbulence statistics. Moreover, the minimum of the autocorrelation function along the spanwise direction is negative, demonstrating that the computational box is large enough to contain at least two streaks, and provide acceptable near-wall turbulence statistics.
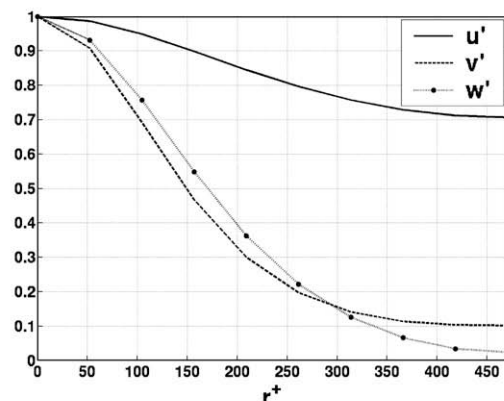
In anisothermal flows, density and viscosity variations make the classical *log*-law no more valid [8]. To account for temperature gradient, the following dimensionless variables are introduced [5,23–25]:
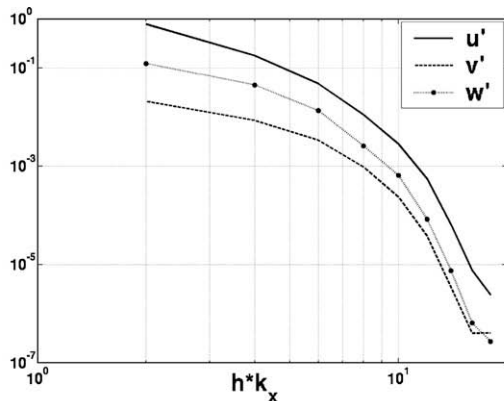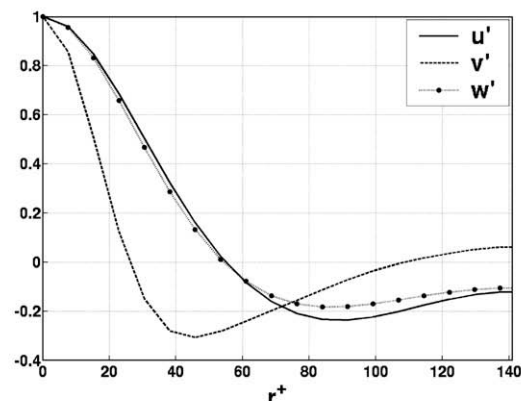
(a) Spatial velocity power spectra, along the x-direction at $y^+ = 30$.
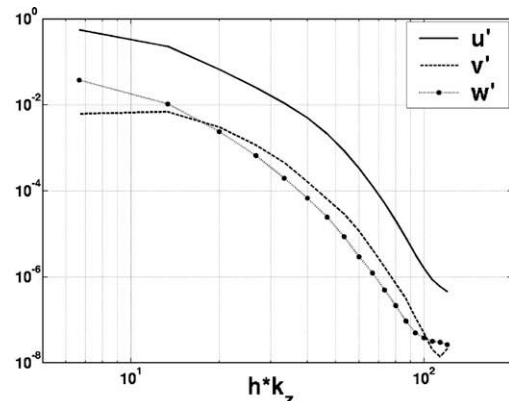
(b) Spatial velocity power spectra, along the z-direction at $y^+ = 30$.

(c) Two-point spatial autocorrelation function, along the x-direction ($r^+ = \Delta x^+$) at $y^+ = 5.5$.

(d) Two-point spatial autocorrelation function, along the z-direction ($r^+ = \Delta z^+$) at $y^+ = 5.5$.

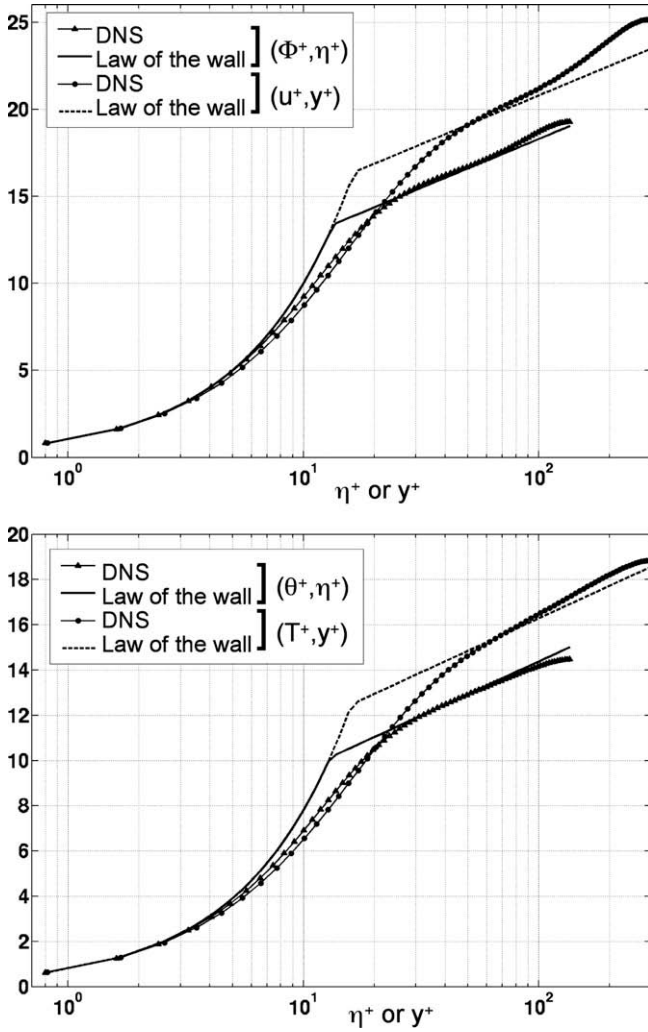Fig. 4. Near-wall turbulence statistics for the anisothermal flow.

Fig. 5. Mean streamwise velocity (top) and temperature (bottom) expressed in wall units ($\bar{u}^+, \bar{T}^+, y^+$) and in LnKc variables ($\bar{\phi}^+, \bar{\theta}^+, \eta^+$).

$$\eta^+ = \frac{v^s}{v} y^+, \quad \bar{\phi}^+ = \frac{\bar{\rho}}{\bar{\rho}^s} u^+, \quad \bar{\theta}^+ = \frac{\bar{\rho}}{\bar{\rho}^s} \bar{T}^+ \tag{7}$$

with:

$$\bar{T}^+ = -\frac{(\bar{T} - \bar{T}^s) \bar{\rho}^s \overline{C}_p u_\tau}{\bar{\varphi}^s} \tag{8}$$

where $\overline{C}_p$ and $\bar{\varphi}^s$ denote respectively the mean mass specific heat capacity at constant pressure and the mean heat flux from the gas to the wall. Kays et al. [5] showed that these new variables, called LnKC variables in [23], allowed to recover the classical logarithmic profile in the inertial zone of the boundary layer for both the velocity and the temperature. Fig. 5 shows the mean velocity and the mean temperature profiles expressed in both classical wall units and LnKC variables. The distance of the laminar–turbulent transition is now located at $y_{lt}^+ = 16.4$, to be compared to the $y_{lt}^+ = 11.6$ value obtained in the isothermal case, while the shear velocity and the laminar kinematic viscosity at the wall have passed from $u_\tau = 2.75$ m s^{-1} and $v^s = 1.17 \, 10^{-5}$ m s^{-1} to $u_\tau = 2.06$ m s^{-1} and $v^s = 1.63 \, 10^{-5}$ m s^{-1} in the anisothermal case. In other words y_{lt} is twice and half larger in the anisothermal case. As expected a logarithmic behavior is recovered with the LnKC variables. The additive constants in the *log*-laws and therefore the laminar–turbulent transition differ from those obtained by Angelberger [26] but are in agreement with the results of Nicoud [3] and Huang & Coleman [4], who suggest that these
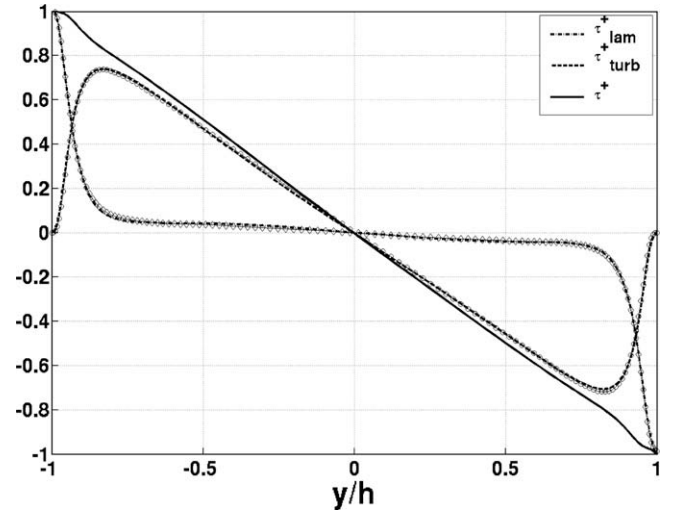

Fig. 6. Normalized shear stress profiles for the anisothermal case (lines). For comparison, symbols represent the isothermal case.

parameters depend on the heat flux parameter $B_q = \bar{\varphi}^s / \bar{\rho}^s \overline{C}_p u_\tau \bar{T}^s$. In the present DNS, this flux parameter is found to be equal to $B_q = 0.0354$, leading to the following laws of the wall:

$$\text{Dynamic}: \begin{cases} \eta^+ \leqslant 13.4 : \bar{\phi}^+ = \eta^+ \\ \eta^+ \geqslant 13.4 : \bar{\phi}^+ = 2.44 \, ln(\eta^+) + 7.07 \end{cases} \tag{9}$$

$$\text{Thermal}: \begin{cases} \eta^+ \leqslant 13.0 : \bar{\theta}^+ = Pr \, \eta^+ \\ \eta^+ \geqslant 13.0 : \bar{\theta}^+ = 2.075 \, ln(\eta^+) + 4.82 \end{cases} \tag{10}$$

Fig. 6 shows that the shear stress profiles in the anisothermal and isothermal flows are almost identical, indicating that the temperature variation acts on the flow dynamics mainly through the density and the viscosity. In addition, the total shear stress τ^+ behaves as a linear function of the normal coordinate y^+ if density is taken into account as follows:

$$\tau^+ = \tau_{turb}^+ + \tau_{lam}^+ = -\rho^+ \overline{u'v'}^+ + \rho^+ v^+ \frac{\partial \bar{u}^+}{\partial y^+} = -\frac{y^+}{h^+} \tag{11}$$

where $\rho^+ = \bar{\rho}/\bar{\rho}^s$ and $v^+ = v/v^s$.

6. Channel flow with evaporating liquid films

In this section, evaporating liquid films are added on the top and bottom walls. Five different cases are considered. They are defined by the liquid surface temperature T^s and the target gas flow conditions in terms of velocity U_{target}, temperature T_{target} and fuel mass fraction $Y_{F,target}$. These operating conditions are summarized in Table 4. Note that case 3 corresponds to the anisothermal case of the previous section. To cover a wide range of evaporation rate, the liquid film surface temperature T^s increases from 309.4 K in case 1 to 370 K in case 5, a value close to the boiling temperature of *n*-heptane. Different values for the gas temperature are also used to reach different temperature gradients at the surface of the liquid film. It is worth noting that in case 4, T_{target} is smaller than T^s leading to a negative gradient. The fuel mass fraction $Y_{F,target}$ is strongly increased from 0.1 in case 1 to 0.6 in case 4, while going back to a low value in case 5. Because of the heptane viscosity, that is about one order of magnitude lower than the air viscosity, the resulting gas mixture viscosity decreases from case 1 to case 4, and the channel height h is also decreased to keep a Reynolds number Re at approximately the same value for all cases. As a consequence, the number of grid points in the vertical y-direction is accordingly adjusted to keep a good resolution.

Table 4
Definition of the five cases.

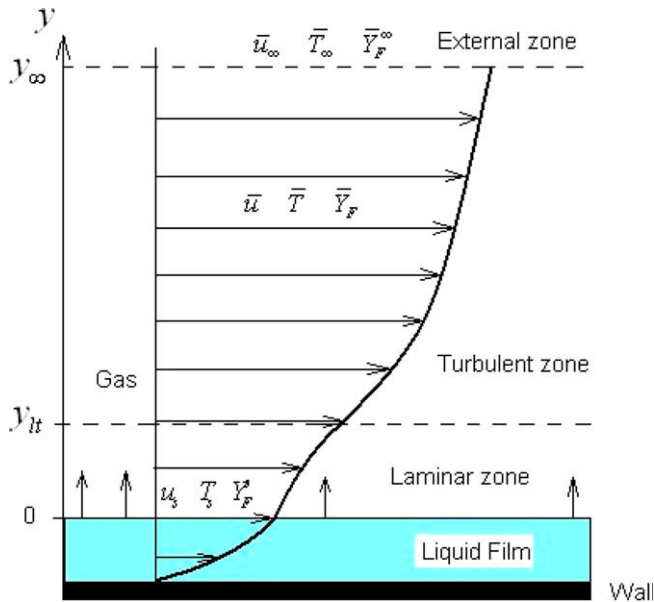| Variable	Case 1	Case 2	Case 3	Case 4	Case 5
T^s (K)	309.4	333.0	360.0	368.0	370.0
T_{target} (K)	400	500	600	320	500
U_{target} (m s^{-1})	50	50	50	50	50
$Y_{F.target}$	0.1	0.2	0.2	0.6	0.2
h (m)	1.2382 e^{-3}	1.5612 e^{-3}	2.0936 e^{-3}	3.3485 e^{-4}	1.7239 e^{-3}
Re	2560	2710	2750	2760	3100
Grid	22 × 155 × 44	22 × 172 × 43	22 × 176 × 44	22 × 150 × 44	22 × 196 × 44

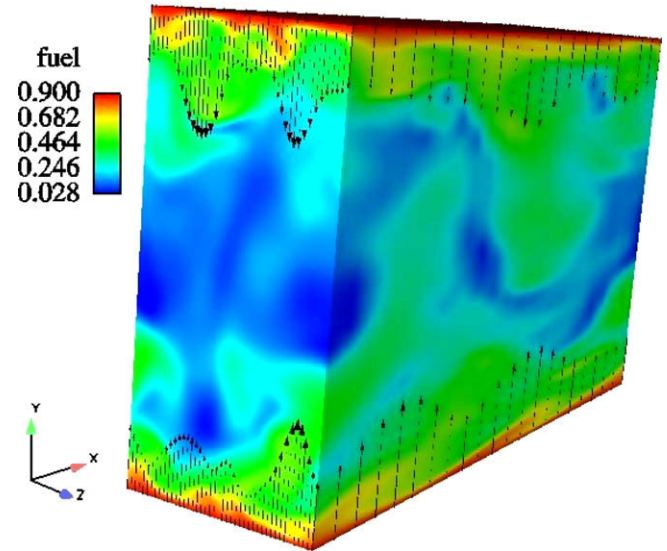**Fig. 7.** Structure of the boundary layer above a liquid film.

Fig. 8. Field of fuel mass fraction and Stephan velocity for case 4.

Table 5
Characteristics of the five cases.

Variable	Case 1	Case 2	Case 3	Case 4	Case 5
$\overline{T}_c$ (K)	401.9	503.2	598.2	319.1	499.3
$\overline{P}_c$ (Pa)	99,860	99,750	100,640	101,840	101,960
$\overline{U}_c$ (m s^{-1})	48.2	51.7	50.4	51.6	50.0
$\overline{Y}_{F,c}$	0.097	0.189	0.210	0.560	0.237
Y_F^s	0.30	0.60	0.90	0.98	0.99
u_τ (m s^{-1}]	2.04	1.52	0.60	0.69	0.26
Re_τ	242	374	351	96	196
Δy_w^+	0.92	0.89	0.76	0.41	0.27
$\overline{\varphi^s}$ [kJ m^{-2} s^{-1}]	17.2	24.4	9.93	−3.58	1.36
$\overline{v_S}^+$	0.01	0.035	0.249	1.164	1.508
$\overline{M}$ (g m^{-2} s^{-1})	28.9	96.3	402	2540	1290

Fig. 9. Mean streamwise velocity profiles expressed in wall units ($\bar{u}^+, y^+$).

The values of the operating conditions actually reached during the simulations are summarized in Table 5. The actual values of the channel centerline gas temperature $\overline{T}_c$, pressure $\overline{P}_c$, velocity $\overline{U}_c$ and composition $\overline{Y}_{F,c}$ are reported, and are found close to the specified target values (Table 4). The values of Y_F^s reported in Table 5 are functions not only of T^s but also of the mean molecular weight of the mixture W^s at the liquid surface. They are found to increase from 0.3 in case 1 to 0.99 in case 5. The friction velocity u_τ decreases from 2.04 m s^{-1} in case 1 to 0.26 m s^{-1} in case 5, leading to a reduction of the first cell size at the surface of the liquid δy_w^+. All values of δy_w^+ are lower than one, therefore in good adequacy with the grid refinement required in the viscous sublayer. Finally, the flow is actually fully turbulent for all cases as indicated
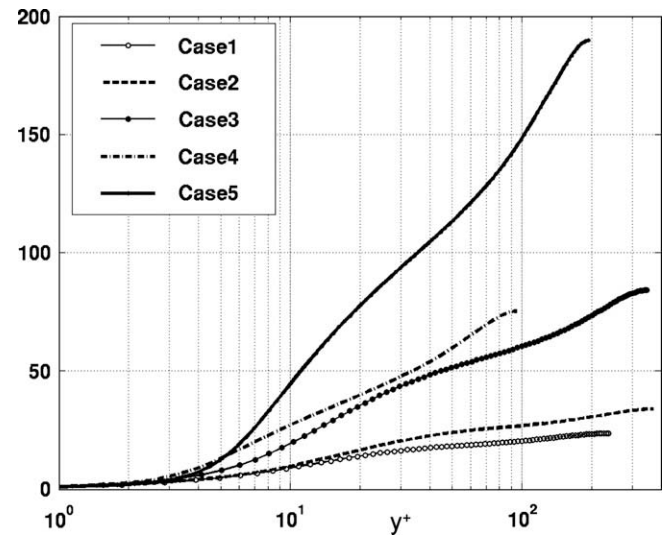
by the Reynolds number Re_τ. Even if case 4 has a lower Re_τ, the energy power spectra and autocorrelation functions have been checked to ensure sufficiently accurate statistics.

Table 5 also displays mean values of the liquid–gas heat flux $\overline{\varphi^s} = \overline{(\lambda \partial T/\partial y)^s}$ and mass flux $\overline{M}$, as well as the mean Stephan velocity. It appears clearly that these two quantities are not directly correlated and that the evaporation of a liquid film is not a function of the heat flux only. In particular the laminar Schmidt

number has a direct impact on the mass flux and varies from 1.4496 in case 1 to 0.2486 in case 5, leading to a strong increase of the Stephan velocity from case 1 to case 5. In this last case, Sc is about three times smaller than Pr. The heat flux is directly linked to the temperature difference between the liquid surface and the gas but it is modulated by the Stephan velocity that decreases the temperature gradient. Another impact of the blowing Stephan velocity is to significantly reduce the friction velocity, leading to a value of 0.6 m s^{-1} in case 3, to be compared to the 2.06 m s^{-1} in the corresponding non evaporating anisothermal case of the previous section, and down to 0.26 m s^{-1} in case 5. The behaviour of these parameters illustrates the complexity of the boundary layer physical processes under the influence of an evaporating liquid film.

6.1. Flow analysis

Fig. 8 shows a view of the 3D fuel mass fraction with the Stephan velocity at the film surface for the case 4. Injected at the film surface with a varying injection velocity equal to the Stephan velocity, the fuel vapor gradually fills the channel through turbulent mixing and diffusion. The profiles of the mean streamwise velocity expressed in wall units $(\bar{u}^+, y^+)$ is plotted in Fig. 9 for the five cases. One important observation is that they do not remain logarithmic in the fully turbulent region of the boundary layer. It is also difficult to identify a clear transition between the viscous sublayer and the inertial zone. Moreover, cases 1 and 5 differ by one order of magnitude on $\bar{u}^+$, but one should keep in mind
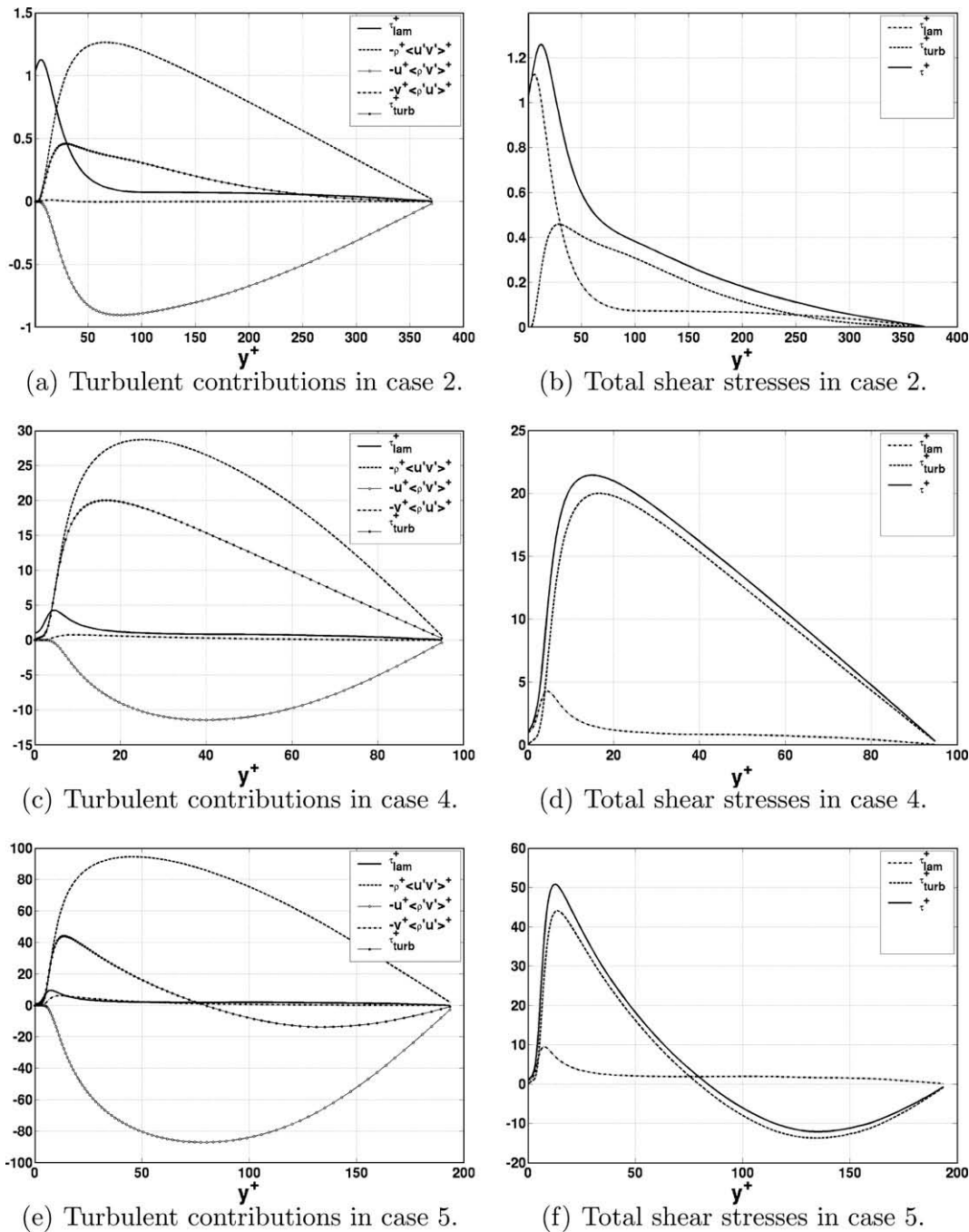

(a) Turbulent contributions in case 2.

(b) Total shear stresses in case 2.

(c) Turbulent contributions in case 4.

(d) Total shear stresses in case 4.

(e) Turbulent contributions in case 5.

(f) Total shear stresses in case 5.

Fig. 10. Contributions to the total shear stress. Comparison of cases 2, 4 and 5.

that this is mainly due to the strong variation of u_τ (see Table 5). The total shear stress expressed in wall units writes in the evaporating case:

$$\tau^+ = \rho^+ \nu^+ \frac{\partial \bar{u}^+}{\partial y^+} - \left[\bar{\rho}^+ \overline{u'\nu'}^+ + \bar{u}^+ \overline{\rho'\nu'}^+ + \bar{\nu}^+ \overline{\rho'u'}^+ \right] = \tau^+_{lam} + \tau^+_{turb}$$

(12)

where two extra terms $\bar{u}^+ \overline{\rho'\nu'}^+$ and $\bar{\nu}^+ \overline{\rho'u'}^+$ appear in the turbulent part, due to the non-zero transverse velocity ν^+ and density fluctuations ρ' due to the liquid film evaporation. Fig. 10a, c and e show the different contributions to the total shear stress for cases 2, 4 and 5. If the term $\bar{\nu}^+ \overline{\rho'u'}^+$ is negligible most of the time, the term $-\bar{u}^+ \overline{\rho'\nu'}^+$ becomes high enough to compensate for the classical turbulent shear stress term $\bar{\rho}^+ \overline{u'\nu'}^+$. Its contribution seems to increase when the normal density gradient at the film surface are high compared to the normal velocity: indeed the smallest ratio $\bar{u}^+ \overline{\rho'\nu'}^+ / \bar{\rho}^+ \overline{u'\nu'}^+$ is obtained for case 4 where evaporation is very strong but the density gradient is rather weak compared to cases 2 and 5 (see Table 5). The total shear stress, with the turbulent and laminar contributions are gathered In Fig. 10b, d and f. The total shear stress profile τ^+ is not linear in any evaporating case and is found to be maximum inside the boundary layer above the liquid film surface, while it was always maximum at the walls in the non evaporating cases. The location y^+_{lt} where the turbulent shear stress τ^+_{turb} becomes dominant compared to the laminar shear stress τ^+_{lam} comes closer to the surface of the liquid for higher rate of evaporation. For instance, $y^+_{lt} < 5$ is obtained for strong $\dot{M}$ in cases 4 and 5 while $y^+_{lt} > 30$ for rather weak $\dot{M}$ in case 2 (see Table 5). This strong dependence of the boundary layer structure on evaporation rate is an additional difficulty in the derivation of accurate wall functions for a broad range of evaporation rates.

Normalized velocity fluctuations are shown in the Fig. 11 for the five cases. The higher values compared to the isothermal case are due to the lower values of u_τ. When normalized by the same friction velocity u_{τ_0} of the isothermal case, the velocity fluctuations recover values of the same order of magnitude than in non evaporating cases, with a maximum close to the isothermal case for the streamwise velocity and approximately double for the two other components [27]. However, the location and the width of the peak vary, being broader for stronger evaporation rate and density gradient. These results confirm the modification of the boundary layer structure and are in conformity with the already observed changes of the maxima of the shear stresses τ^+_{turb} and τ^+_{lam} above the liquid film surface. Furthermore, Fig. 11b shows that the normal and spanwise velocity fluctuations increase with the Stephan velocity (see Table 5), but in case 1 they are smaller than in the isothermal case. This is again a consequence of the density and viscosity gradients that compensate the effects of a weak evaporation rate.

The normalized temperature fluctuation T^+_{rms} defined by:

$$T^+_{rms} = \sqrt{\overline{T'^2}} \left| \frac{\rho^s C_p u_\tau}{\varphi^s} \right|$$

(13)

and the normalized fuel mass fraction fluctuation $Y^+_{F_{rms}}$ defined by:

$$Y^+_{F_{rms}} = \frac{\sqrt{\overline{Y'^2_F}}}{(1 - Y^s_F)\overline{\nu_S}^+}$$

(14)

are shown on Fig. 12. Both quantities behave like the normalized streamwise velocity (Fig. 11), with maximum heat and mass flux localised above the liquid film surface. The maximum levels of T^+_{rms} are also close to the streamwise velocity fluctuations levels. This is not true for $Y^+_{F_{rms}}$ (Fig. 12b) that shows already higher values in cases 1 and 2, due to the low value of the Stephan velocity. Note that the Stephan velocity behaves like $1/Sc$ while φ^s behaves like
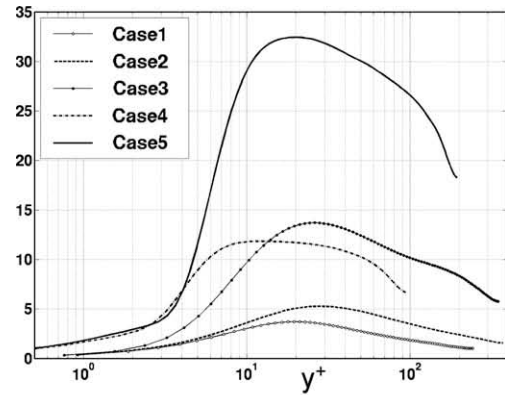
(a) Streamwise velocity fluctuations.
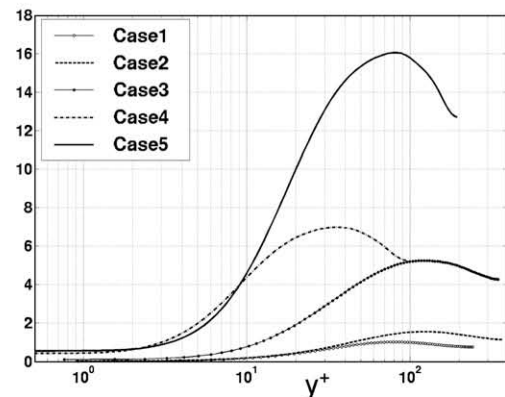
(b) Normal velocity fluctuations.
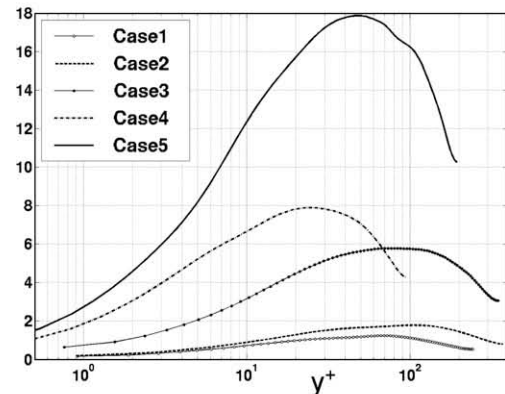
(c) Spanwise velocity fluctuations.

Fig. 11. Normalized streamwise, normal and spanwise velocity fluctuations for the liquid film evaporating cases.

$1/Pr$, and that Sc varies significantly from cases 1 to 5 while Pr is a constant. This explains the different behaviors of the temperature and fuel mass fraction fluctuations. For example in case 5, where Sc is about three times smaller than Pr, $Y^+_{F_{rms}}$ is also about three times smaller than T^+_{rms}.

The vorticity fluctuations normalized by u_τ^2/ν^s (Fig. 13) appear to be much higher than in the isothermal case and increase from cases 1 to 5, i.e. with the Stephan velocity and the density and viscosity gradients. This is again partly explained by the disparity of u_τ^2/ν^s, that is about two times higher in case 4 than in case 3. According to Fig. 13, the Stephan velocity seems to accentuate the hollows and bumps of the streamwise vorticity fluctuations (cases 4 and 5) whereas the density and viscosity gradients seem
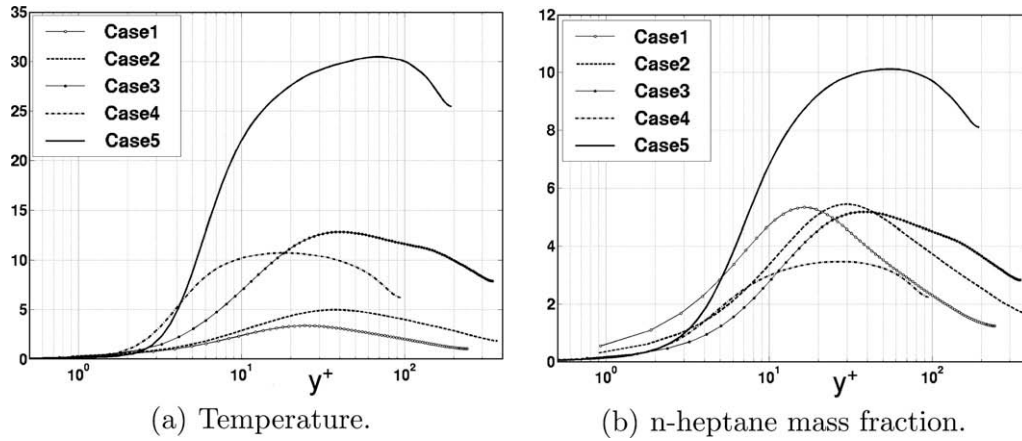
(a) Temperature.　　　　(b) n-heptane mass fraction.

Fig. 12. Normalized fluctuations of temperature and mass fraction for the liquid film evaporating cases.

to smooth them (case 3) as was also the case in the anisothermal flow. A more detailed comparison with the anisothermal case shows that the shape of the normal vorticity fluctuations profiles is similar in all cases (with and without evaporation), except near the liquid film surface where the slope of the curves is smaller for higher evaporation. On the contrary, the spanwise vorticity fluctuations are significantly modified by evaporation, with a peak appearing between the liquid film surface and $y^+ = 10$, increasing with evaporation and density gradients. It corresponds to the location of the peak of laminar shear stress above the liquid–gas interface as already seen in Fig. 10a, c and e. In order to measure the dependency of the evaporation rate to the spanwise vorticity, a correlation factor $F\nu\Omega_z$ is defined as follows:

$$F\nu\Omega_z = \frac{\overline{v'.\Omega_z'}}{\sqrt{\overline{v'^2}.\overline{\Omega_z'^2}}} \tag{15}$$

where Ω_z is the z-component of the vorticity vector. This factor is plotted on Fig. 14. It appears to be high (close to 1 at the liquid film surface) for weak evaporation (cases 1 and 2). It then decreases when the evaporation rate increases (case 3), and even becomes negative for the strongest evaporation cases (4 and 5). A look at instantaneous fields of spanwise vorticity and normal velocity at the bottom liquid film surface illustrates and confirms the strong correlation for weak evaporation rate in case 2 (Fig. 15a and b) and the low correlation for strong evaporation rate in case 4 (Fig. 15c and d). In this last case the negative values may be explained by the occurence of negative spanwise vorticity whereas it always stays positive in weak or medium evaporation cases (1, 2 and 3).

6.2. Wall functions modelling

The presence of an evaporating liquid film changes significantly the behavior of the boundary layer as highlighted in the previous section as detailed in Fig. 7. A fuel vapor mass fraction boundary layer builds up above the liquid film and must be represented by an additional mass wall function, in a similar way to the classical dynamic and thermal law-of-the-walls. Under the influence of an evaporating liquid film, it is clear from Fig. 9 that the mean streamwise velocity profiles expressed in classical wall units do not follow the classical dynamic wall function. Going back to the mean gas momentum equation, and assuming incompressiblity and negligible pressure gradient, one obtains for steady conditions and statistical mean variables:

$$\bar{v}\frac{\partial\bar{u}}{\partial y} = \frac{\partial}{\partial y}\left[(v + v_t)\frac{\partial\bar{u}}{\partial y}\right] \tag{16}$$

where v_t is the turbulent viscosity, modelled as:

$$v_t = \left(\frac{Ky}{C_u}\right)^2\frac{\partial\bar{u}}{\partial y} \tag{17}$$

where K is the Karmann constant and C_u is a model constant to be determined. Integrating and using $\bar{v} = \bar{v}_S$ from mass conservation equation, one obtains:

$$\bar{u}\bar{v}_S = v\frac{\partial\bar{u}}{\partial y} + \left(\frac{Ky}{C_u}\frac{\partial\bar{u}}{\partial y}\right)^2 + K_1 \tag{18}$$

The integration constant K_1 is obtained from the evaluation of $\bar{u}$ at $y = 0$:

$$\overline{u^s}\overline{v_S} = \left(v\frac{\partial\bar{u}}{\partial y}\right)^s + K_1 = u_\tau^2 + K_1 \tag{19}$$

Normalizing $\bar{u}$ as $\bar{u}^+ = (\bar{u} - \bar{u}^s)/u_\tau$ one finally gets:

$$\bar{u}^+\overline{v_S}^+ = \frac{\partial\bar{u}^+}{\partial y^+} + \left(\frac{Ky^+}{C_u}\frac{\partial\bar{u}^+}{\partial y^+}\right)^2 - 1 \tag{20}$$

In the laminar sublayer, i.e. between $y^+ = 0$ and $y^+ = y_{lt}^+$, it is assumed that $v_t << v$, so that Eq. (20) reduces to:

$$\bar{u}^+\overline{v_S}^+ = \frac{\partial\bar{u}^+}{\partial y^+} - 1 \tag{21}$$

that admits the solution $\overline{u}^+\overline{v_S}^+ = exp(\overline{v_S}^+y^+) - 1$, approximated for small values of y^+ by $\bar{u}^+ = y^+$. In the inertial sublayer, i.e. for $y^+ > y_{lt}^+$, it is assumed that $v << v_t$, and Eq. (20) now reduces to:

$$\overline{u}^+\overline{v_S}^+ = \left(\frac{Ky^+}{C_u}\frac{\partial\overline{u}^+}{\partial y^+}\right)^2 - 1 \tag{22}$$

which leads to the classical logarithmic wall function for the mean streamwise velocity:

$$\bar{u}_{eff}^+ = \frac{C_u}{K}ln\left(\frac{y^+}{y_{lt}^+}\right) + y_{lt}^+ \tag{23}$$

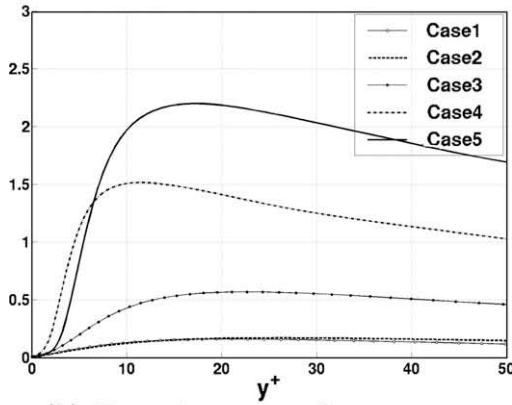where a new wall effective velocity variable is defined as follows:

$$\bar{u}_{eff}^+ = \frac{2}{\overline{v_S}^+}\left[\sqrt{1 + \overline{u}^+\overline{v_S}^+} - 1\right] \tag{24}$$

Note that in the laminar sublayer, the approximation $\bar{u}_{eff}^+ = y^+$ still holds.
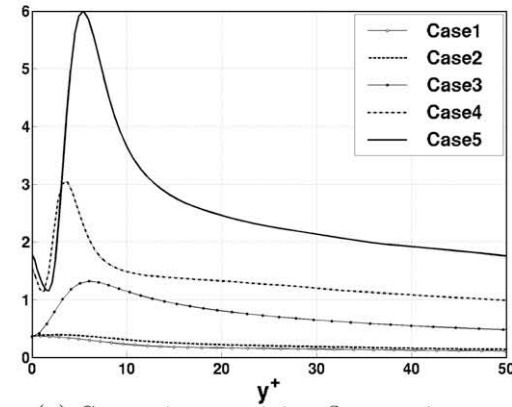
The same methodology may be used for the derivation of the wall functions of the temperature and the fuel mass fraction, for
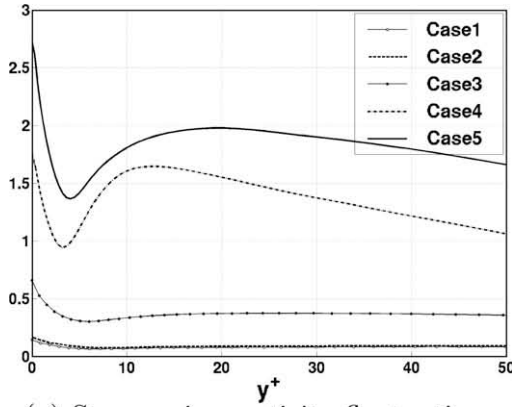
(a) Streamwise vorticity fluctuations.

(b) Normal vorticity fluctuations.

(c) Spanwise vorticity fluctuations.

Fig. 13. Normalized vorticity fluctuations for the liquid film evaporating cases.

which the mean equations of energy and fuel mass fraction are written respectively:

$$\bar{v}\frac{\partial \overline{T}}{\partial y} = \frac{\partial}{\partial y}\left[(\alpha + \alpha_t)\frac{\partial \overline{T}}{\partial y}\right] \tag{25}$$

and

$$\bar{v}\frac{\partial \overline{Y_F}}{\partial y} = \frac{\partial}{\partial y}\left[(D + D_t)\frac{\partial \overline{Y_F}}{\partial y}\right] \tag{26}$$

where the same assumptions as for the velocity have been made, and where $\alpha = v/Pr$ and $D = v/Sc$ are respectively the heat and molecular laminar diffusion coefficients. The turbulent values are modelled as
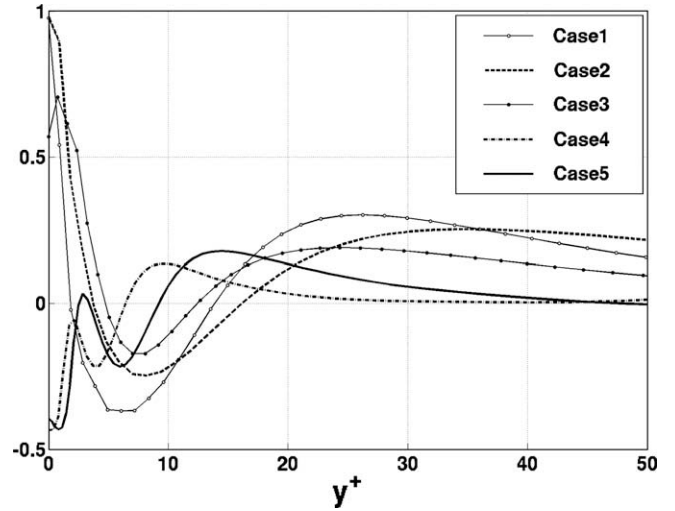

Fig. 14. Correlation factor of the normal velocity and the spanwise vorticity.

$\alpha_t = v_t/(C_T Pr_t) = K^2 y^2/(C_u^2 C_T Pr_t)(\partial \bar{u}/\partial y)$ and $D_t = v_t/(C_Y Sc_t) = K^2 y^2/(C_u^2 C_Y Sc_t)(\partial \bar{u}/\partial y)$, where C_T and C_Y are model constants and $Pr_t = 0.9$ and $Sc_t = 0.9$ denote respectively the turbulent Prandtl and Schmidt numbers. A first integration gives:

$$\overline{T}\,\overline{v_S} = \left(\frac{v}{Pr} + \frac{K^2 y^2}{C_u^2 C_T Pr_t}\frac{\partial \bar{u}}{\partial y}\right)\frac{\partial \overline{T}}{\partial y} + \overline{T^s}\,\overline{v_S} - \frac{\bar{\varphi}^s}{\bar{\rho}^s \overline{C_p}^s} \tag{27}$$

and

$$\overline{Y_F}\overline{v_S} = \left(\frac{v}{Sc} + \frac{K^2 y^2}{C_u^2 C_Y Sc_t}\frac{\partial \bar{u}}{\partial y}\right)\frac{\partial \overline{Y_F}}{\partial y} + \overline{v_S} \tag{28}$$

Normalizing $\overline{T}$ as $\overline{T}^+ = -(\overline{T} - \overline{T}^s)u_\tau \bar{\rho}^s \overline{C_p}^s/\bar{\varphi}^s$ and $\overline{Y_F}$ as $\overline{Y_F}^+ = (\overline{Y_F} - 1)/(\overline{Y_F}^s - 1)$, the two above equations may be rewritten in non-dimensional wall variables:

$$\overline{T}^+\overline{v_S}^+ = \left(\frac{1}{Pr} + \frac{K^2 y^{+2}}{C_u^2 C_T Pr_t}\frac{\partial \bar{u}^+}{\partial y^+}\right)\frac{\partial \overline{T}^+}{\partial y^+} - 1 \tag{29}$$

and

$$\overline{Y_F}^+\overline{v_S}^+ = \left(\frac{1}{Sc} + \frac{K^2 y^{+2}}{C_u^2 C_Y Sc_t}\frac{\partial \bar{u}^+}{\partial y^+}\right)\frac{\partial \overline{Y_F}^+}{\partial y^+} \tag{30}$$

In the laminar sublayer, one finds easily $\overline{T}^+\overline{v_S}^+ = exp(\overline{v_S}^+y^+Pr) - 1$ and $\overline{Y_F}^+\overline{v_S}^+ = exp(\overline{v_S}^+y^+Sc)$, which can be approximated for small values of y^+ by $\overline{T}^+ = Pr\ y^+$ and $\overline{Y_F}^+ = Sc\ y^+$ respectively. In the inertial sublayer, replacing $\partial \bar{u}^+/\partial y^+$ by its expression from Eqs. (22) and (23) and integrating leads to:

$$\frac{1 + \overline{T}^+\overline{v_S}^+}{1 + \overline{T}^+(y_{lt}^+)\overline{v_S}^+} = \left[1 + \frac{C_u\overline{v_S}^+ln(y^+/y_{lt}^+)}{2K(1 + \overline{v_S}^+y_{lt}^+/2)}\right]^{2Pr_t C_T} \tag{31}$$

and

$$\frac{\overline{Y_F} - 1}{\overline{Y_F}(y_{lt}^+) - 1} = \left[1 + \frac{C_u\overline{v_S}^+ln(y^+/y_{lt}^+)}{2K(1 + \overline{v_S}^+y_{lt}^+/2)}\right]^{2Sc_t C_Y} \tag{32}$$

As a consequence the wall temperature and mass fraction variables are re-defined as:

$$\overline{T}_{eff}^+ = \frac{2C_T Pr_t}{\overline{v_S}^+}\left[\left(1 + \overline{T}^+\overline{v_S}^+\right)^{1/2C_T Pr_t} - 1\right] \tag{33}$$

$$\overline{Y_F}_{eff}^+ = \frac{2C_Y Sc_t}{\overline{v_S}^+}\left[\left(\overline{Y_F}^+\right)^{1/2C_Y Sc_t} - 1\right] \tag{34}$$

(a) Spanwise vorticity for case 2.

(b) Normal velocity for case 2.

(c) Spanwise vorticity for case 4.
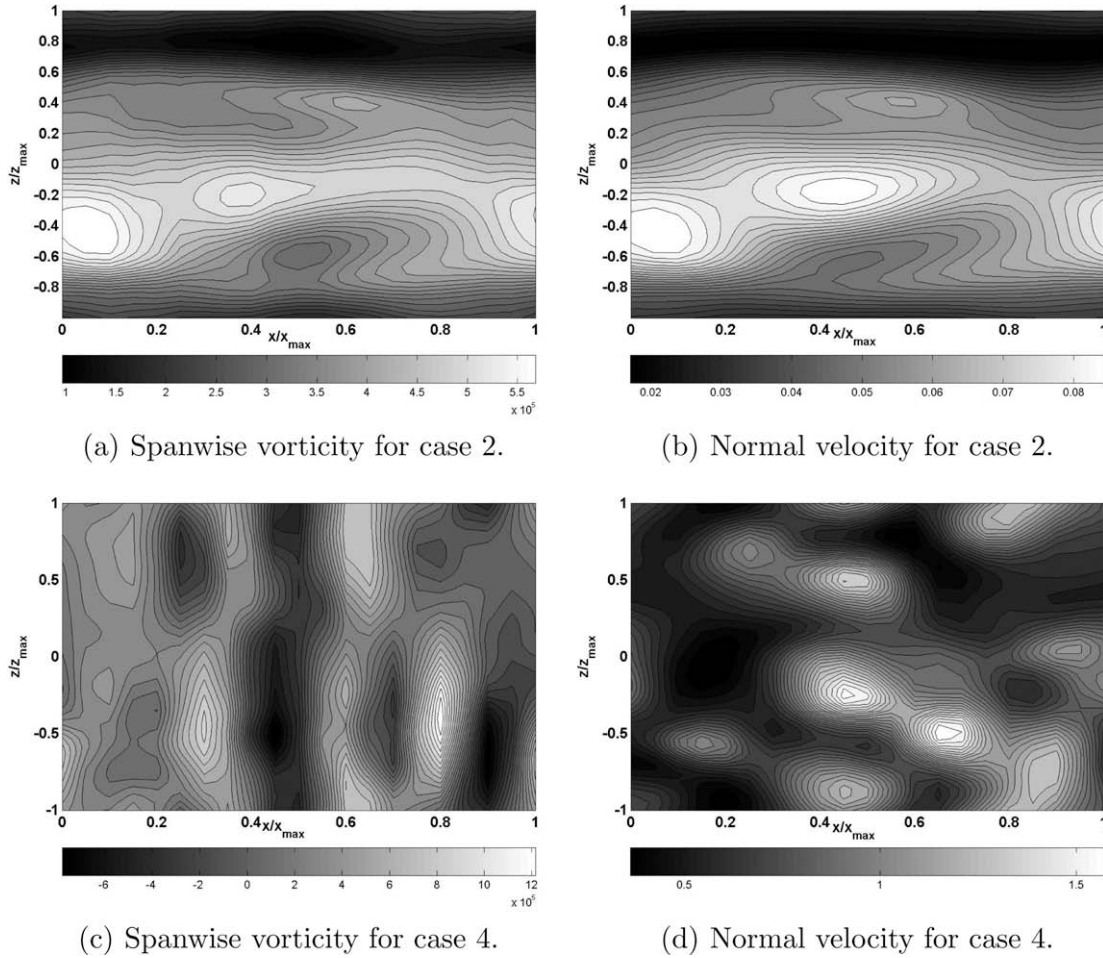

(d) Normal velocity for case 4.

Fig. 15. Instantaneous field of spanwise vorticity and normal velocity at the bottom liquid film surface for case 2 and 4.

With these new effective variables, the profiles of mean streamwise velocity, temperature and fuel mass fraction become almost logarithmic in the fully turbulent boundary layer. These new definitions also decrease the differences between cases 1 and 5, reducing them to density and viscosity variations as has been shown by Desoutter [27]. These effective variables are finally associated to the LnKc definitions [26], to obtain the effective LnKc variables:

$$\eta^+ = \frac{v^s}{v} y^+, \quad \bar{\phi}_{eff}^+ = \frac{\bar{\rho}}{\bar{\rho}^s} \bar{u}_{eff}^+, \quad \bar{\theta}_{eff}^+ = \frac{\bar{\rho}}{\bar{\rho}^s} \bar{T}_{eff}^+, \quad \bar{\zeta}_{eff}^+ = \frac{\bar{\rho}}{\bar{\rho}^s} \overline{Y}_{F\,eff}^+ \quad (35)$$

Using these definitions and the previous expressions for u_{eff}^+, T_{eff}^+ and $Y_{F\,eff}^+$, one can derive the following new wall functions:
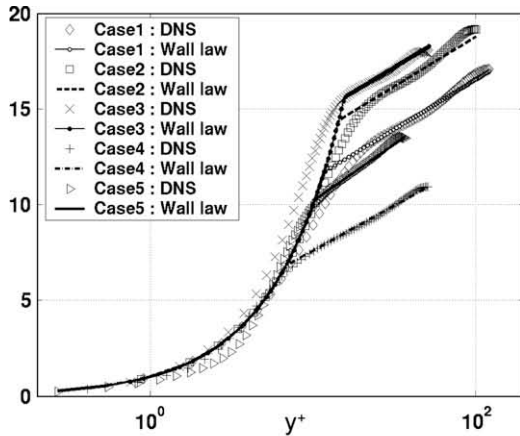
$$Dynamic: \begin{cases} \eta^+ \leqslant \eta_{lt}^+ : \bar{\phi}_{eff}^+ = \eta^+ \\ \eta^+ \geqslant \eta_{lt}^+ : \bar{\phi}_{eff}^+ = \eta_{lt}^+ + \frac{C_u}{K} \ln \frac{\eta^+}{\eta_{lt}^+} \end{cases} \quad (36)$$

$$Thermal: \begin{cases} \eta^+ \leqslant \eta_{lt,T}^+ : \bar{\theta}_{eff}^+ = Pr\, \eta^+ \\ \eta^+ \geqslant \eta_{lt,T}^+ : \bar{\theta}_{eff}^+ = Pr\, \eta_{lt,T}^+ + \frac{C_u}{K} \left[\frac{2C_T Pr_t + Pr \overline{v_S}^+ \eta_{lt,T}^+}{2 + \overline{v_S}^+ \eta_{lt,T}^+} \right] \ln \frac{\eta^+}{\eta_{lt,T}^+} \end{cases} \quad (37)$$
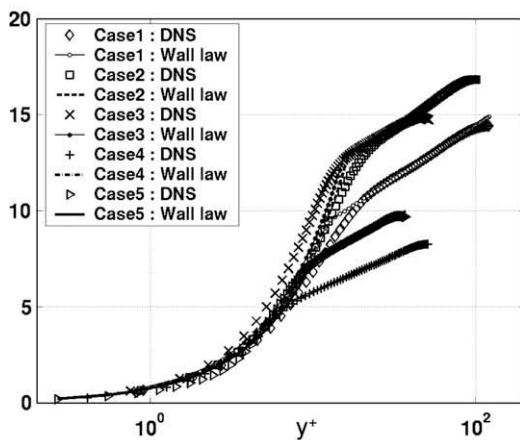
$$Mass: \begin{cases} \eta^+ \leqslant \eta_{lt,Y}^+ : \bar{\zeta}_{eff}^+ = Sc\, \eta^+ \\ \eta^+ \geqslant \eta_{lt,Y}^+ : \bar{\zeta}_{eff}^+ = Sc_{lt} \eta_{lt,Y}^+ + \frac{C_u}{K} \left[\frac{2C_Y Sc_t + Sc_{lt} \overline{v_S}^+ \eta_{lt,Y}^+}{2 + \overline{v_S}^+ \eta_{lt,Y}^+} \right] \ln \frac{\eta^+}{\eta_{lt,Y}^+} \end{cases} \quad (38)$$

where η_{lt}^+, $\eta_{lt,T}^+$ and $\eta_{lt,Y}^+$ are the distances from the liquid film surface to the laminar-turbulent transition, respectively for the dynamic, the thermal and the fuel mass fraction boundary layers. They are
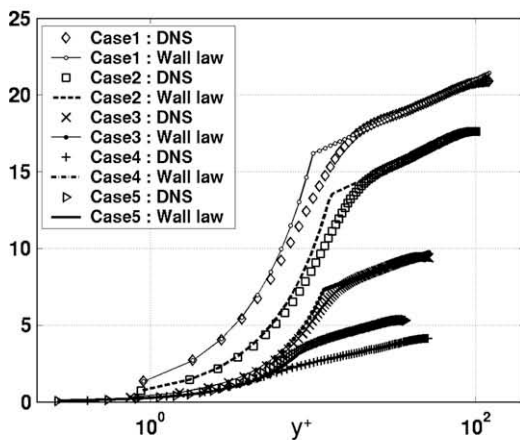
determined by identification of the wall functions to the DNS profiles. The Schmidt number Sc_{lt} is calculated using Eq. (5) at the location of the laminar-turbulent transition. Fig. 16 shows the comparison between the calculated profiles and the above wall functions (Eqs. (36)–(38)). The values of the different constant parameters obtained by fitting these wall functions to the DNS results are summarized in Table 6. Except in the buffer zone between the two sublayers, the new wall functions match closely the DNS results. A classical logarithmic behavior in the fully turbulent zone is obtained. In addition, the assumption of linear evolution in the laminar zone is well verified. As shown in Table 6, the fitted parameters used in the wall functions are not constant and vary with the evaporation rate and density gradient. However the variations of C_u, C_T and C_Y never exceed 30% and may be taken in the range of 0.9-1.1, 1.21-1.26 and 1.0-1.3 respectively. Concerning the laminar-turbulent transition locations, a first observation is that the three parameters η_{lt}^+, $\eta_{lt,T}^+$ and $\eta_{lt,Y}^+$ are close for each individual case, allowing to use one single value for the three wall laws. However they strongly differ for the five cases, ranging approximatively between 7 and 15, with lower values corresponding to higher evaporation rates and lower density gradients. Furthermore, it is worth noting that, going back to dimensional values, $y_{lt}, y_{lt,T}$ and $y_{lt,Y}$ increase with both evaporation and density gradient, since this behaviour corresponds to a decrease of the friction velocity u_τ. Finally, it is important to note that in the limit of small evaporation rate and gradients of density and viscosity, the wall functions (Eqs. (36)–(38)) reduce to the standard wall functions [28].

(a) Mean streamwise velocity.

(b) Mean temperature.

(c) Mean n-heptane mass fraction.

Fig. 16. Wall functions expressed in new effective LnKc variables ($\bar{\phi}^+_{eff}, \bar{\theta}^+_{eff}, \bar{\zeta}^+_{eff}, \eta^+$). Comparison to the DNS results.

Table 6
Fitted parameters of the wall laws.

Variables	Case 1	Case 2	Case 3	Case 4	Case 5
η^+_{lt}	11.7	14.4	15.6	6.80	10.2
$\eta^+_{lt,T}$	12.6	16.3	15.5	7.00	9.85
$\eta^+_{lt,m}$	10.0	12.8	11.6	6.87	9.37
C_u	0.973	0.973	0.962	0.884	1.110
C_T	1.212	1.257	1.223	1.212	1.257
C_Y	1.000	1.023	1.000	1.312	1.301

thermal and fuel mass fraction boundary layers. Major changes in the structure of the boundary layer were observed under the combined influence of the rate of evaporation and the gradients of density and viscosity induced by the presence of fuel vapor in the gas mixture. In particular, it was shown that:

- All mass, momentum and energy fluxes at the surface of the liquid film are strongly decreased by the gradients of density and by the blowing of the boundary layer by evaporation.
- The maximum of the shear stress is moved towards the interior of the boundary layer by the Stephan velocity induced by evaporation.
- The viscous sublayer thickens with the increase of the gradients of density, viscosity and the rate of evaporation.

In addition, it was shown that the heat and mass flux between the liquid and the gas resulting from evaporation undergoes strong fluctuations linked to the gas flow turbulence. Their average value is used to develop new wall variables that include the effects of density, mass and temperature gradients at the film surface ad allow to build new wall functions to describe the boundary layer. These new wall functions were confronted to the DNS results to check their validity and accuracy. In particular the constant parameters that appear in the derivation were adjusted from the DNS. They may be directly used in CFD codes to take into account the effect of the presence of a liquid film, as was done by Desoutter [27].

References

[1] T. Schönfeld, M. Rudgyard, Steady and unsteady flows simulations using the hybrid flow solver AVBP, AIAA J. 37 (11) (1999) 1378–1385.
[2] J. Kim, P. Moin, R. Moser, Turbulence statistics in fully developed channel flow at low Reynolds number, J. Fluid Mech. 177 (1987) 133–166.
[3] F. Nicoud, G. Winckelmans, D. Carati, J. Baggett, W. Cabot, Boundary conditions for LES away from the wall, in: Summer Program, Center for Turbulence Research, 1998, pp. 413–422.
[4] P. Huang, G. Coleman, Van driest transformation and compressible wall-bounded flows, AIAA J. 32 (10) (1994) 2110–2113.
[5] W.M. Kays, M. Crawford, Convective Heat and Mass Transfer, McGraw Hill, 2004.
[6] F. Nicoud, J. Angilella, Effects of uniform injection at wall on the stability of Couette-like flows, Phys. Rev. E 56 (3) (1997) 3000–3009.
[7] S. Mendez, F. Nicoud, LES of a turbulent flow around a perforated plate, in: CY-LES, Limassol, Cyprus, 2005.
[8] T. Poinsot, D. Veynante, in: R.T. Edwards (Ed.), Theoretical and Numerical Combustion, second ed., 2005.
[9] L. Artal, F. Nicoud, Direct numerical simulation of reacting turbulent multi-species channel flow, in: Proceedings of the 6th International ERCOFTAC Workshop – Direct and Large-Eddy Simulation, Université de Poitiers, France, 2005, pp. 85–92.
[10] T. Alshaalan, C. Rutland, Turbulence, scalar transport and reaction rates in flame wall interaction, Proc. Combust. Inst. 27 (1998) 793–799.
[11] G. Bruneaux, K. Akselvoll, T. Poinsot, J. Ferziger, Flame-wall interaction in a turbulent channel flow, Combust. Flame 107 (1/2) (1996) 27–44.
[12] L. Artal, S. Mendez, F. Nicoud, Using direct numerical simulations to develop wall functions, in: ENUMATH 05 – Minisymposium on Multisacle Methods in CFD, Santiago de Compostella, Spain, 2005.
[13] H. Schlichting, Boundary Layer Theory, McGraw-Hill, New York, 1955.
[14] U. Piomelli, P. Moin, P. Ferziger, Large eddy simulation of the flow in a transpired channel, J. Thermophys. 5 (1) (1991) 124–128.
[15] Y. Sumitani, N. Kasagi, Direct numerical simulation of turbulent transport with uniform wall injection and suction, AIAA J. 33 (7) (1995) 1220–1228.

7. Conclusions

In this paper, the physical processes that occur in the turbulent boundary layer when subjected to the influence of an evaporating liquid fuel film (n-heptane) were investigated. Several DNS of the "minimal channel" flow configuration were carried out with and without a liquid film on walls. The results allowed to identify the important parameters governing the behaviour of the dynamic,

[16] J. Jimenez, P. Moin, The minimal flow unit in near-wall turbulence, J. Fluid Mech. 225 (1991) 213–240.

[17] A. Roux, L. Gicquel, Y. Sommerer, T. Poinsot, Large eddy simulation of mean and oscillating flow in side-dump ramjet combustor, Combust. Flame 152 (1–2) (2008) 154–176.

[18] P. Schmitt, T. Poinsot, B. Schuermans, K. Geigle, Large-eddy simulation and experimental study of heat transfer, nitric oxide emissions and combustion instability in a swirled turbulent high pressure burner, J. Fluid Mech. 570 (2007) 17–46.

[19] C. Martin, L. Benoit, Y. Sommerer, F. Nicoud, T. Poinsot, LES and acoustic analysis of combustion instability in a staged turbulent swirled combustor, AIAA J. 44 (4) (2006) 741–750.

[20] L. Selle, L. Benoit, T. Poinsot, F. Nicoud, W. Krebs, Joint use of compressible large-eddy simulation and Helmoltz solvers for the analysis of rotating modes in an industrial swirled burner, Combust. Flame 145 (1–2) (2006) 194–205.

[21] O. Colin, M. Rudgyard, Development of high-order Taylor–Galerkin schemes for unsteady calculations, J. Comput. Phys. 162 (2) (2000) 338–371.

[22] A. Ern, V. Giovangigli, Multicomponent Transport Algorithms, Lecture Notes in Physics, Springer-Verlag, Heidelberg, 1994.

[23] C. Angelberger, T. Poinsot, B. Delhaye, Improving near-wall combustion and wall heat transfer modelling in SI engine computations, in: Int. Fall Fuels & Lub. Meeting & Exposition, SAE Paper 972881, Tulsa, 1997.

[24] Z. Han, R. Reitz, F. Corcione, G. Valentino, Interpretation of $k - epsilon$ computed turbulence length scale predictions for engine flows, in: 26th Symposium (Int.) on Combustion, The Combustion Institute, Pittsburgh, 1996, pp. 2717–2723.

[25] K. Truffin, A. Benkenida, A temperature fluctuation equation model dedicated to the computation of turbulent thermal layers in high reynolds internal flows, Int. J. Heat Mass Transfer 51 (21–22) (2008) 5160–5174.

[26] C. Angelberger, Contributions à la modélisation de l'interaction flamme-paroi et des flux pariétaux dans les moteurs à allumage commandé, Ph.D. thesis, PSA peugeot-Citroën et CERFACS (1997).

[27] G. Desoutter, Etude numérique de la propagation d'une flamme sous l'influence d'un film liquide de carburant sur une paroi, Ph.D. thesis, Institut National Polytechnique de Toulouse (2007).

[28] B. Launder, D. Spalding, The numerical computation of turbulent flows, Comput. Meth. Appl. Mech. Eng. 3 (1974) 269–289.